RESEARCH ARTICLE

Three-dimensional reconstruction of helicopter blade–tip vortices using a multi-camera BOS system

André Bauknecht · Benjamin Ewers · Christian Wolf · Friedrich Leopold · Jianping Yin · Markus Raffel

Abstract Noise and structural vibrations in rotorcraft are strongly influenced by interactions between blade–tip vortices and the structural components of a helicopter. As a result, knowing the three-dimensional location of vortices is highly desirable, especially for the case of full-scale helicopters under realistic flight conditions. In the current study, we present results from a flight test with a full-scale BO 105 in an open-pit mine. A background-oriented schlieren measurement system consisting of ten cameras with a natural background was used to visualize the vortices of the helicopter during maneuvering flight. Vortex filaments could be visualized and extracted up to a vortex age of 360°. Vortex instability effects were found for several flight conditions. For the camera calibration, an iterative approach using points on the helicopter fuselage was applied. Point correspondence between vortex curves in the evaluated images was established by means of epipolar geometry. A three-dimensional reconstruction of the main part of the vortex system was carried out for the first time using stereophotogrammetry. The reconstructed vortex system had good qualitative agreement with the result of an unsteady free-wake panel method simulation. A quantitative evaluation of the 3D vortex system was carried out, demonstrating the potential of the multi-camera background-oriented schlieren measurement technique for the analysis of blade–vortex interaction effects on rotorcraft.

A. Bauknecht (✉) · B. Ewers · C. Wolf · M. Raffel
Helicopter Department, Institute of Aerodynamics and Flow Technology, German Aerospace Center (DLR), Bunsenstr. 10, 37073 Göttingen, Germany
e-mail: andre.bauknecht@dlr.de

F. Leopold
French-German Research Institute (ISL), 5 rue du Général Cassagnou, 68300 Saint-Louis, France

J. Yin
Helicopter Department, Institute of Aerodynamics and Flow Technology, German Aerospace Center (DLR), Lilienthalplatz 7, 38108 Braunschweig, Germany

1 Introduction

The intensive research in the area of blade–tip vortices of full-scale helicopter rotors (Wadcock et al. 2011; Heineck et al. 2013; Bauknecht et al. 2014b; Raffel et al. 2014) reflects the importance of improving our understanding of how helicopters generate noise. In addition to the detailed aerodynamic characterization of single vortex filaments for young vortex ages (Kindler et al. 2011; Wadcock et al. 2011), the determination of the exact location and orientation of the entire vortex system in three-dimensional (3D) space is of great importance. The interaction of blade–tip vortices with the fuselage of the helicopter or the rotor blades, also referred to as blade–vortex interaction (BVI), plays a significant role in the generation of noise and structural vibrations, see e.g., Hardin and Lamkin (1987). BVI noise is caused by the interaction of a rotor blade with a previously generated vortex from another rotor blade. These vortex–blade encounters happen during unsteady maneuvers such as descending forward flight, when the vortex filaments convect close to the rotor tip path plane. The passing vortex filament causes changes in the local blade aerodynamics and high unsteady pressure fluctuations on the interacting blade. The magnitude of this interaction effect primarily depends on the strength of the vortex, as well as its distance and orientation to the interacting rotor blade (see Hardin and Lamkin 1987 for details).

A number of sub-scale experimental (Splettstoesser et al. 1997; van der Wall et al. 2004) and numerical

studies (Lim and Strawn 2008; van der Wall 2012; Kutz et al. 2013) have been conducted in order to examine the BVI effect for 3D helicopter configurations. In general, these studies return qualitatively converging results for the positions and orientations of the blade–tip vortices. In detail, however, the results still exhibit significant scattering and a strong dependency on the respective boundary or experimental conditions. The prediction of BVI is difficult due to the large number of underlying and interacting effects, such as blade aerodynamics including the lift time history, blade aeroelasticity, fuselage-interference, atmospheric conditions, and overall aircraft performance and trimming, see Hardin and Lamkin (1987). Correctly scaling or computationally reproducing all of these influences is challenging. The study of full-scale vortex trajectories under real flight conditions, however, provides the information essential for the validation of numerical simulations and sub-scale experiments. To date, only a few studies are available which focus on the reconstruction of blade–tip vortices on a small part of a full-scale helicopter (Klinge et al. 2006; Heineck et al. 2013) or the detection of blade–tip vortices on a full-scale helicopter in maneuvering flight (Bauknecht et al. 2014a, b; Raffel et al. 2014).

In the current paper, we present results from measurements with a full-scale BO 105 helicopter operated under unsteady flight conditions and out of ground effect. A 10-camera background-oriented schlieren (BOS) system with a natural background was used to visualize and, for the first time, to reconstruct the main part of the rotor blade–tip vortex system in 3D space.

2 Materials and methods

2.1 The background-oriented schlieren technique

Schlieren-based methods have a long tradition in flow diagnostics. They visualize and quantify the spatial gradient of the fluid's density ρ, which manifests as an optical distortion due to alteration of the refractive index n as described by the Gladstone–Dale equation

$$n - 1 = K \cdot \rho, \qquad (1)$$

where K is the Gladstone–Dale constant. The BOS method provides a simple experimental setup that is suitable for full-scale applications. The underlying principles of the standard BOS approach is taken from Richard and Raffel (2001) and will only be outlined briefly here.

A digital camera is focused on a background pattern, with the phase object (i.e., density gradient) located in the line-of-sight, see Fig. 1. The corresponding refractions of the light rays evoke apparent shifts of the background, which can be evaluated by comparison to a reference image
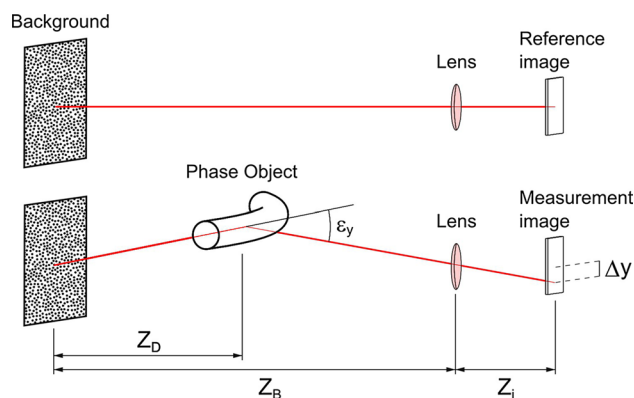

Fig. 1 Principle of the standard BOS setup with an artificial background from Bauknecht et al. (2014b). For reasons of clarity, only the deflection in y direction is depicted

using well-known cross-correlation algorithms as described by Raffel et al. (2007). The angular deflection ϵ_y due to a variation in the refractive index n can be written as (Venkatakrishnan and Meier 2004):

$$\tan(\epsilon_y) = \int_0^{Z_B} \frac{1}{n} \frac{\partial n}{\partial y} dz \qquad (2)$$

Hence, the method yields an integral measure of the density gradients along the line-of-sight z. From a practical point of view, the best results are achieved for spatially delimited density variations (as in case of tip vortices) embedded in an undisturbed, homogeneous environment. Assuming small deflection angles, the displacement Δy in the image plane is expressed as

$$\Delta y = Z_D M \epsilon_y, \qquad (3)$$

with the background magnification factor $M = Z_i/Z_B$, focal length Z_i, distance between the density variation and the background Z_D and distance between the camera lens and the background Z_B.

Given a single camera with a rotationally symmetrical phase object or multiple cameras observing an unsymmetrical phase object from different perspectives, the 3D density field can also be reconstructed from the 2D displacements Δy, see Venkatakrishnan and Meier (2004). Application of the density reconstruction is limited to highly spatially resolved phase objects, as the spatial averaging effect of the cross-correlation evaluation decreases the displacement magnitudes and consequently the integrated density differences within the measurement domain. With the objective of resolving the entire vortex system, no reconstruction of the density field was carried out in the present study.

The cross-correlation routine favors backgrounds with small-scale structures resulting in a high spatial resolution. Furthermore, a high contrast of the background results in a high signal-to-noise ratio and allows for small

exposure times. For laboratory environments, these conditions are usually met by printing random dot patterns on retro-reflective screens, with a dot diameter and a dot density adapted to the camera resolution. The application of artificial background patterns is also feasible for full-scale test cases in outdoor environments, see e.g., Raffel et al. (2014). However, this approach requires huge background screens which are impracticable and expensive, especially for multi-camera setups.

Alternatively, natural backgrounds can also be utilized for BOS, as shown by Kindler et al. (2007). Natural background structures, such as scree formations in mountain environments, provide appropriate conditions, combined with minimal preparation and low cost (see Bauknecht et al. 2014b for a comparison of natural background structures). The choice of a natural background, however, must fulfill several requirements. First, the background structure needs to be time-constant between the acquisition of the reference and the measurement image. Thus care must be taken when using vegetated areas (in case of wind gusts), and to avoid changes of the illumination (i.e., relocation of clouds and shadows). Variations in the background can be accommodated for the case of unsteady or moving phase objects by taking double-image pairs with short separation times, also attributed to as 'reference-free' BOS (Raffel et al. 2000; Bauknecht et al. 2014b). Second, the background must cover the entire region of interest, which favors large-scale stepped or sloped terrains.

In addition to the planar projection of the phase object, the volumetric shape and location can also be investigated by using a multi-camera BOS setup with (at least) two cameras. For both stereoscopic and multi-camera setups, the cameras must be positioned to image the phase object from different perspectives with large angles between the cameras, e.g., 90° for a stereoscopic setup. For each camera, a background pattern has to be located behind the measurement object, requiring a large background with a semicircular outline ('amphitheater'). For full-scale measurements with natural backgrounds, this complicates the search for suitable test sites.

To date, two studies by Klinge et al. (2006) and Heineck et al. (2013) have used the stereoscopic BOS technique for the spatial reconstruction of full-scale helicopter blade–tip vortices. The studies were conducted on a hovering helicopter (Klinge et al. 2006) and a full-scale rotor in a wind tunnel (Heineck et al. 2013) and both focused on a small part of the vortex system. In the present paper, a multi-camera BOS approach for the reconstruction of a large part of the vortex system of a full-scale helicopter is presented for the first time.

2.2 Experimental setup

An open-pit chalk mine in the Harz Mountains in Germany, which met the requirements for the natural background, was chosen as a test site, see Fig. 2. The background (shown in Fig. 3a) consisted of a naturally illuminated slope with a semicircular layout and a height of about 45 m. The background featured favorable structures for BOS imaging, including scree and small rocks. The full-scale helicopter is depicted within the measurement volume in the lower right corner of Fig. 2. The approximately
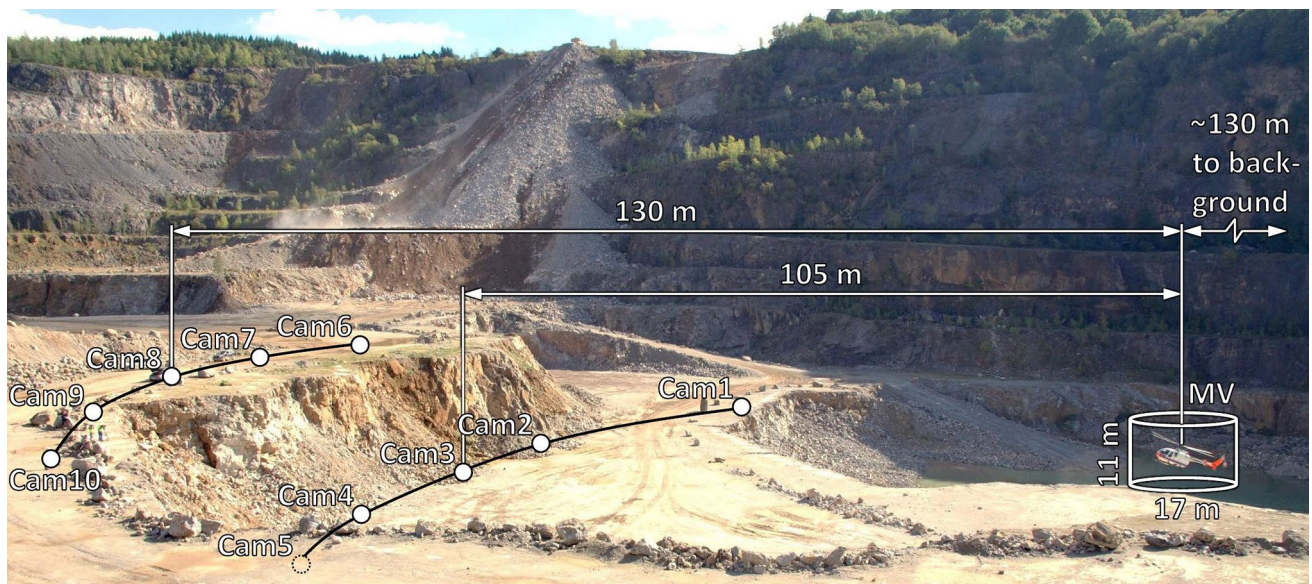

Fig. 2 Photograph of the measurement setup with marked positions of the ten cameras, the measurement volume (MV), and the helicopter. The natural background is located to the right and outside of the image
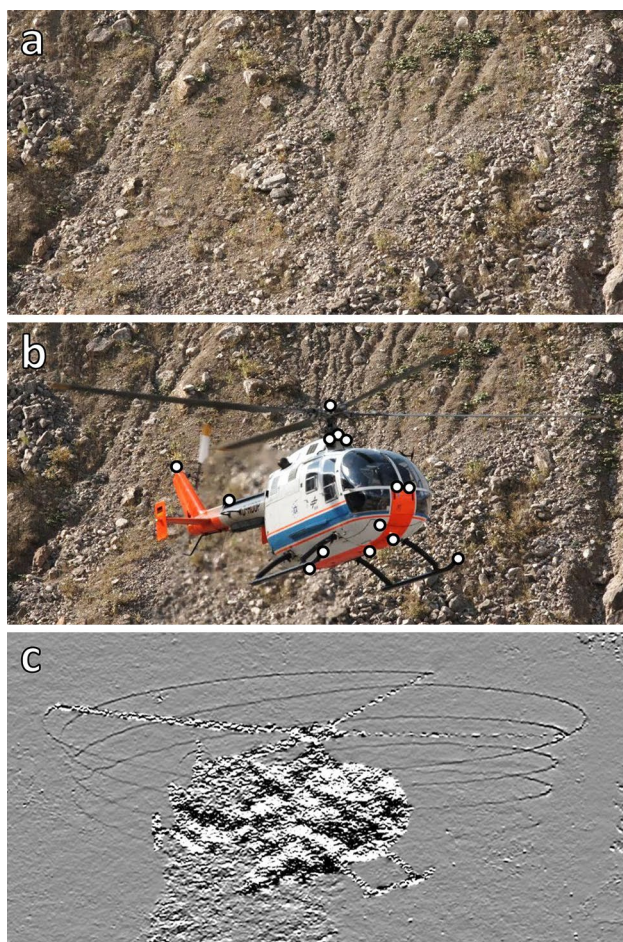
Fig. 3 Cutouts of **a** the reference image, **b** the measurement image with selected points for the camera calibration, and **c** the resulting vertical displacement gradient field from the cross-correlation of **a** and **b**

cylindrical measurement volume, i.e., the overlapping field of view of the cameras, had a diameter of 17 m and a height of 11 m. Schlieren images were taken by a system of ten digital single-lens reflex cameras in order to visualize the tip vortices of the full-scale BO 105 in both hovering flight and under unsteady flight conditions. The cameras were positioned at distances of $(Z_B - Z_D) = 105 - 140$ m to the helicopter and $Z_B = 230 - 300$ m to the background. The pit contained two floor levels with a vertical separation of 15 m. Five cameras were positioned on the upper floor level and five cameras on the lower level. The setup covered a horizontal angle of $80°$ and a vertical angle of $6°$ between the outermost cameras. The position of individual cameras was chosen to optimize the background coverage, resulting in an unevenly distributed camera setup (see camera 1 in Fig. 2).

The camera system consisted of Nikon D7100 cameras featuring 24 Mpx CMOS image sensors which were equipped with Nikkor 55–300 mm zoom lenses and

connected to a cable-based triggering system. The triggering of the camera system had a camera-inherent, random jitter of about 0.5 ms. The zoom lenses were adjusted to provide a similar resolution of about 0.34 px/mm within the measurement volume, requiring focal lengths Z_i of between 150 and 195 mm. Exposure times were set to 1 ms for all cameras with ISO values of 400. The aperture sizes of the camera lenses were adapted to the natural illumination of the corresponding background and varied between $f/5.6$ and $f/11$. During the measurements, sunny and windless weather conditions were present with an ambient temperature of about $15°C$ and wind velocities of less than 1 m/s.

2.3 Test helicopter and maneuvers

The flight tests were conducted with an MBB BO 105 helicopter from DLR Brunswick, as shown in Fig. 3b. The twin-engine, multi-purpose helicopter has a four-bladed ($N_b = 4$) hingeless rotor with square blade–tips and a radius of $R = 4.92$ m, a chord length of $c = 0.27$ m, and a solidity of $\sigma = N_b c/(\pi R) = 0.07$. The blades rotated at an angular velocity of $\Omega = 44.4$ rad/s, which corresponds to a hover tip Mach number of $Ma_t = 0.64$. The helicopter was manned with two pilots and a radio operator and had a take-off weight of about 2,300 kg during the test runs. In order to fly unsteady maneuvers, the helicopter had to generate thrust in the range of $T = 23–28$ kN, corresponding to a thrust coefficient of $C_T = T/(\rho \pi \Omega^2 R^4) = 0.005 - 0.006$ and a blade loading of $C_T/\sigma = 0.07 - 0.09$.

For the flight tests, the helicopter was flown into the open-pit mine. The relatively small measurement volume as well as the steep slopes on all sides of the mine restricted the possible flight maneuvers to hovering flight and unsteady swinging motions along the vertical (ascent/ descent) and longitudinal axis (pitching maneuver) of the helicopter to simulate unsteady maneuvering loads. During the test runs, the helicopter was operated primarily within the measurement volume, while performing maneuvers with translation amplitudes of up to 10 m and fuselage pitch angles of up to $30°$.

3 Two-dimensional vortex visualization

3.1 BOS evaluation

The measurement principle of the BOS technique requires undisturbed reference images without the helicopter, as shown in Fig. 3a, to be acquired immediately before and/ or after each test run. The time difference between acquisition of the measurement images (Fig. 3b) and the reference images has to be kept as small as possible (<5–10 min) in

Fig. 4 Photograph of the BO 105 during a swinging maneuver, acquired by camera 2. The displacement gradient field is overlaid, depicting the tip vortex positions

order to minimize changes in the background that result from measuring in an outdoor environment with natural illumination, such as moving shadows or drying of wet surfaces. As an initial processing step after the image acquisition, both reference and measurement images were converted to gray scale based on luminance preservation. The measurement images were mapped onto the reference images using a de-warping algorithm to correct for possible camera translations and rotations during the image acquisition. This de-warping algorithm is based on the displacements in the corners of the image pairs, as determined via cross-correlation. A transformation matrix is then calculated based on these displacements and used to correct the measurement image. Sectional cross-correlation of the mapped image pairs was carried out using a commercial PIV software (Davis 8.1, LaVision). A multi-grid evaluation scheme with a final window size of 16×16 pixels, and an overlap of 75 % was selected to resolve the small vortex-induced displacements u and v in the horizontal and vertical directions, respectively. In the resulting displacement field, the displacement vectors point toward regions of low density, i.e., the vortex cores. Vortices with peak-to-peak displacements of $\Delta v = 0.15 - 1.5$ pixels and projected diameters of 4–6 pixels were detected in the present study. Robust indicators for the center position of the vortices are given by the spatial gradients $\mathrm{d}u/\mathrm{d}x$ and $\mathrm{d}v/\mathrm{d}y$. These indicators emphasize the vortices due to their high spatial gradients compared with the gradual changes in the surrounding flow field.

An example for the visualization of blade–tip vortices in the 2D camera plane is given in Fig. 3c. Figure 3c shows the result of the sectional cross-correlation between the

reference image (Fig. 3a) and the measurement image containing the BO 105 during an ascending flight maneuver (Fig. 3b). The vortices are visible as dark helically curved lines in front of the gray background. The positions of the helicopter and its rotor blades are indicated by strongly de-correlated regions. Below and behind the helicopter, the noisy area marks the trajectory of the exhaust gases of the two engines.

3.2 Single camera 2D vortex visualization

The capability of the BOS technique to visualize blade–tip vortices is demonstrated by the result shown in Fig. 4. The cropped picture from camera 2 features the BO 105 at the forward reverse point of a swinging motion about the pitch axis of the helicopter. The vertical displacement gradient field, as acquired by cross-correlation with an undisturbed reference image, is overlaid and visualizes a large part of the main rotor vortex system, as labeled with the number "1" in Fig. 4. A maximum vortex age of about $\psi_v \approx 450°$ (corresponding to 1.25 rotor revolutions) can clearly be distinguished from the low background noise level on the advancing blade side, see number "2." In the upper right corner of the image, marked with the number "3," a region with increased background noise occurs, which can be attributed to the presence of a tree in the camera background. The leaves of the tree provide a high contrast for the cross-correlation, but are prone to variations between the acquisition of the reference and measurement image due to the downwash of the helicopter rotor. These variations can be directly observed in Fig. 4 and are superimposed onto the displacements due to the blade–tip vortices,

hindering their detection. The sensitivity and perspective of the optical setup enable for the partial visualization of the tail rotor tip vortices, see number "4." A reconstruction of the tail rotor vortex system was not carried out in this paper, as there were not enough cameras with an unobstructed view of the tail rotor.

Partial obstruction of the vortex system in Fig. 4 is caused by the fuselage, rotor, and engine exhaust, which is observed in the density gradient field behind the BO 105 (labeled with the number "5"). The hot exhaust gases produced by the two engines of the helicopter convect downwards with the rotor flow and form two large plumes that are visible even to the naked eye due to the large optical distortions evoked in the background image (see Fig. 3b). The corresponding image displacements are too large and inhomogeneous for the cross-correlation method to yield meaningful results, thus producing two de-correlated areas in the displacement gradient field, which merge close to the fuselage.

On the retreating blade side of the helicopter, depicted on the right-hand side (r.h.s.) of Fig. 4, the uniform shape of the vortex curves changes around a vortex age of $\psi_v = 180°$ and the onset of vortex instability effects is observed. For vortex ages of between $\psi_v = 180°$ and $\psi_v = 360°$ around the position labeled with number "6," smooth sinuous disturbances are found, as described by Sullivan (1973). This phenomenon frequently occurs for rotors in hovering flight and is characterized by the wavy shape of the vortex filaments with large amplitudes perpendicular to the main vortex axis. This sort of instability pattern is relatively stable with time and can grow in amplitude with wake age, similar to the vortex marked with number "6" and the vortex above it. Instability effects are also found on the advancing blade side, but to a smaller extent and only close to the maximum visible vortex age of $\psi_v = 450°$.

The vortex visualization in Fig. 4 is comparable with similar results from a BOS vortex visualization on a Cougar helicopter in maneuvering flight from Bauknecht et al. (2014b). Good agreement is found for the maximum visible vortex age of 360–450° and the background noise level. The displacement signals of the Cougar's blade–tip vortices were 2–5 times stronger than for the BO 105. The differences is attributed to the increased thrust coefficient of the Cougar of $C_T = 0.01$ compared with $C_T = 0.005$ for the BO 105 and to the optical amplification factor $Z_D \cdot M = 0.32 - 0.4$ m of the previous camera setup, compared with $Z_D \cdot M = 0.1$ m for the current setup (see Eq. 3).

3.3 Vortex extraction

In preparation for the 3D vortex reconstruction, the positions of the 2D blade–tip vortices in all camera planes were extracted from the evaluated displacement images to get the 2D vortex positions in Fig. 5. Since the signal-to-noise ratio in the displacement fields was too low to ensure vortex detection with a fully automated procedure, a semi-automatic detection algorithm was employed to find discrete points on the vortex lines. Starting from user-selected points close to the vortex filaments, the program employed step-wise cross-correlation between cuts orthogonal to the main vortex axis in combination with a polynomial-based predictor. The step size of the algorithm was automatically adapted according to the curvature of the line segment, and small missing segments in the vortex signal were skipped. For larger uncorrelated areas and outliers due to the inhomogeneous background, the vortex positions had to be entered manually. A spline curve was fitted to the discrete points on each vortex filament by means of a least-squares procedure, and the splines were coded by the blade from which they originated and their position relative to the helicopter fuselage. This labeling was necessary to ensure that, for a given point on a 3D vortex filament, the corresponding 2D points on the correct vortex projections in all camera image planes were selected during the point-pairing process before the 3D vortex reconstruction.

The accuracy of the extracted 2D vortex positions is determined by the step size of the cross-correlation algorithm, accuracy of the vortex center detection method, and quality of the spline fit. The maximum deviation between the selected and the actual vortex center positions was therefore conservatively estimated to be below 4 pixels. This value corresponds to a physical distance of 11 mm or $0.04c$.

3.4 Multi-camera 2D vortex visualization

Figure 5 shows six cropped pictures of the BO 105 in ascending hovering flight that were simultaneously acquired by cameras 1–6. The extracted 2D vortex representations are overlaid on their corresponding pictures and color-coded according to the blade from which they originated (front: red, r.h.s.: green, rear: blue, l.h.s.: yellow; positions are in the helicopter frame of reference). In all six depicted camera views, the typical helical shape of the vortex system is observed, featuring a decreasing diameter with wake age, as predicted by the momentum theory. The moderate vertical convection rate close to the rotor disk results in small vertical distances between consequent vortex generations, see e.g., on the right-hand side of camera image 6 in Fig. 5. For older wake ages, the increased vertical convection induces larger distances between consecutive vortex generations. For the lower cameras 1–5, largely continuous vortex lines with a maximum visible vortex age of just above $\psi_v = 360°$ can be detected. The lines are interrupted by the helicopter fuselage and the rotor blades. Further obstruction of the vortex filaments is caused by the
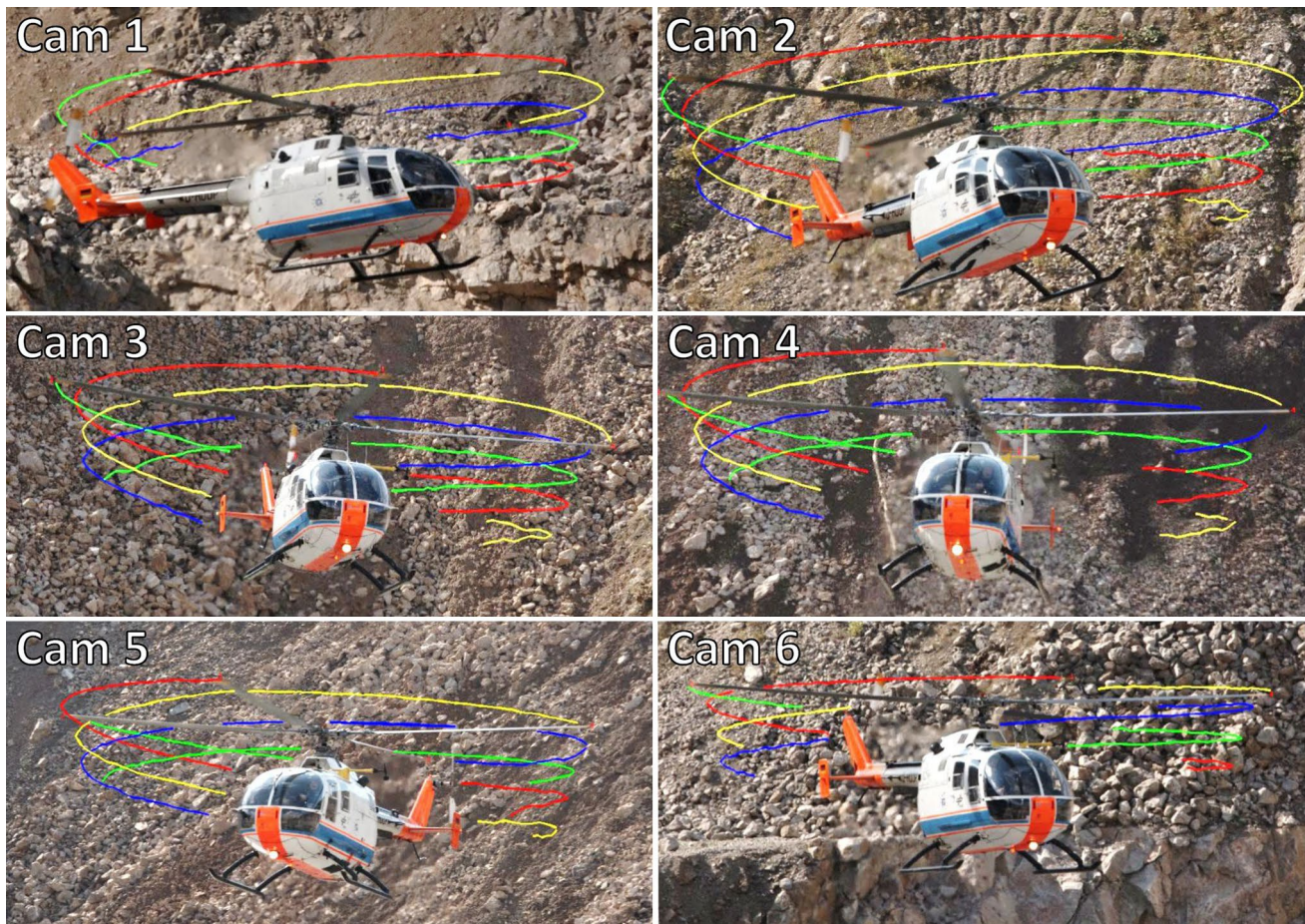
Fig. 5 Photographs of the BO 105 from cameras 1–6 with overlaid extracted 2D tip vortex positions. The vortices are grouped and colorized by the blade from which they originate

hot engine exhaust at the rear of the helicopter and by dark, soil-covered areas in the background, where the image contrast drops to the noise level of the camera sensor (see e.g., Fig 5, camera 4). The main part of the background of the bottom row cameras 1–5 is well suited for the BOS technique, since the background is appropriately illuminated and largely two-dimensional.

The upper level cameras 6–10 have an increased background noise level and a reduced vortex visibility. The maximum detectable vortex age for camera 6 is $\psi_v = 270°$. This elevated background noise is mainly attributed to the large rock formations and lighting problems on the lower half of the imaged slope, leading to increased three-dimensionality of the camera background and shadowing effects. Especially for cameras 8–10, the increased noise level causes a loss of the vortex signal for large parts of the vortex system. Only at the lateral edges of the rotor disk, where the increased integration length through the vortex filaments intensifies the displacement signal, are some vortices visualized. Since the additional information gained by cameras 8–10 is limited, they have been neglected for the

reconstructions carried out in this study. Despite the limitations imposed by the imperfect natural background, a large portion of the main vortex system is visualized using cameras 1–7, which already allows for a better interpretation of the vortex system than for a single camera.

4 Three-dimensional vortex reconstruction

4.1 Camera calibration

Experiments which deal with tomography, holography, or 3D reconstructions depend heavily on the quality of the calibration of the camera system. To estimate the extrinsic camera parameters (Hartley and Zisserman 2003) in a laboratory experiment, a two- or three-dimensional calibration target with a known geometry and position is typically imaged by all cameras of the measurement setup, see Raffel et al. (2007) and Heineck et al. (2013). For full-scale experiments outside the laboratory, as in the present study, the application of a target which covers the entire measurement

volume (i.e., the overlapping field of view of all ten cameras) can pose a significant challenge. For the present test setup, the cylindrical measurement volume was located up to 18 m above the ground with a diameter of 17 m and a height of 11 m. Due to the large dimensions, a different approach was chosen for the camera calibration.

Prior to the test runs, a helium balloon with a diameter of 1 m was positioned inside the measurement volume. All cameras were directed at the balloon and their lens magnifications adjusted to cover approximately the same field of view. A laser distance meter was used to measure the distances and angles between the cameras and the balloon with an accuracy of ±0.5 m. An initial extrinsic camera calibration was calculated from this geometric information and the focal lengths of the cameras. Calibration images of the balloon were acquired for all cameras, and the image coordinates of the balloon center were determined. The differences between the principal points of the cameras and the projected balloon center were used to correct the camera orientations, which deviated from the measured orientations. Lens distortion effects were found to be negligible due to the small ("cropped") camera sensor in combination with an object of interest located close to the image center that covered less than 70 % of the image width.

Naturally, this initial camera calibration was not accurate enough for the reconstruction of vortices with a diameter of less than 0.05 m within the present large fields of view. Therefore, an iterative optimization of the initial camera calibration, with prominent points on the helicopter fuselage, was necessary. A total of 44 points from five different measurement images were manually selected for all ten cameras, as shown by white circular markers in Fig. 3b for one measurement image of camera 2. The accuracy of the manual selection was reduced by the lack of precise marker points and the unsharpness of the helicopter image due to the background-focused cameras. This resulted in an uncertainty of ±2 pixels, corresponding to about ± mm in the physical domain.

For the iterative optimization of the calibration, camera 1 was selected as a master camera and its position and orientation fixed in 3D space. The positions, orientations, and effective focal lengths of the other cameras were iteratively varied. For each camera, paired with the master camera, the helicopter fuselage points were three-dimensionally reconstructed using a triangulation-based stereo photogrammetry technique as described by Mikhail et al. (2001). In principle, a 2D point in the image plane of a camera is projected as a 3D line through the measurement volume using the camera position and orientation in combination with the pinhole camera model. By intersecting the projected lines from a pair of cameras, the 3D coordinates of the corresponding object-space point can be determined. In practice, pairs of lines typically do not intersect in object-space; thus,

the nearest points on the master camera lines with respect to the other lines were chosen as intersection points and the miss distances between line pairs were used as a quality indicator for the convergence of the iterative scheme. For the converged configuration, the cameras were shifted by less than 0.8 m, and the reconstructed points from different cameras typically scattered by less than ±0.03 m.

Although the camera calibration worked sufficiently well for the current evaluation, the use of a large calibration target with known dimensions or automatically detectable markers on the helicopter fuselage could significantly improve the calibration process and increase the calibration accuracy.

4.2 Epipolar geometry

For the 3D reconstruction of a solid object's geometry with photogrammetry, discrete markers or prominent points on its surface have to be imaged and identified in multiple measurement images of the utilized multi-camera system. In order to apply the same reconstruction algorithms to invisible and continuous objects like blade–tip vortices, corresponding points on the vortex lines have to be identified in the images of all cameras (see 'correspondence problem' in Meyn and Bennett 1993). One possible solution for this is the application of the epipolar geometry method, as described by Hartley and Zisserman (2003), which imposes geometric constraints on pairs of camera images, as shown in Fig. 6. Epipolar geometry uses the pinhole camera model and is based on the idea that a plane defined by an object-space point X (e.g., a point on a 3D vortex segment), and its projections X_A and X_B onto the image planes of two cameras (A,B) can be used to establish geometric dependence between X_A and X_B. If only X_A and the corresponding optical center O_A are known, the line through these two points can be projected as an epipolar
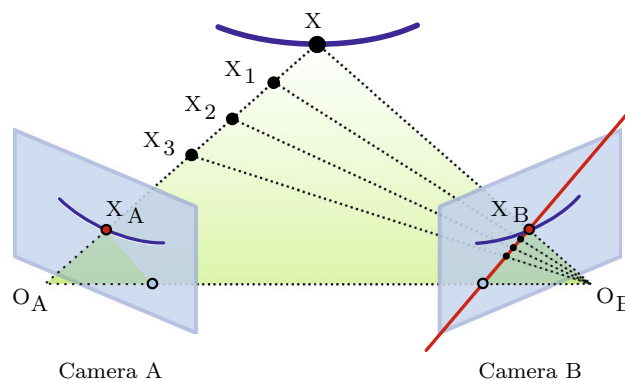

Fig. 6 Epipolar geometry after Heineck et al. (2013), showing the projected camera plane points $\mathbf{X_A}$ and $\mathbf{X_B}$ of the 3D point $\mathbf{X}$ and the corresponding *red epipolar line*

line in the image plane of camera B (see red line in Fig. 6). The projected point X_B corresponding to X_A must be located on this epipolar line. If the vortex that X is located on can be identified in both projections, as shown in Fig. 6, the point X_B can be found by intersecting the epipolar line with the corresponding projected vortex in the image plane of camera B. The constraint imposed by epipolar geometry is written as

$$
\begin{bmatrix} x_A & y_A & 1 \end{bmatrix} \times F \times \begin{bmatrix} x_B \\ y_B \\ 1 \end{bmatrix} = 0, \tag{4}
$$

with the coordinates (x_A, y_A) and (x_B, y_B) of corresponding points in the images A and B and the 3×3 fundamental matrix F. This fundamental matrix can be estimated given at least seven corresponding point pairs in the two images. In the present study, two different methods for the estimation of F were applied, which are both based on point pairs on the helicopter fuselage, as shown in Fig. 3b. These methods are the normalized eight-point algorithm (Hartley 1997) and the random sample consensus (RANSAC, Fischler and Bolles 1981), which was applied to 44 point pairs here. The fundamental matrices were estimated for all possible camera combinations in the present multi-camera setup. The precision of the estimated fundamental matrices was determined by projecting the fuselage points from one camera image as epipolar lines in the corresponding other camera image, where they differed from the respective fuselage points by less than 1.5 pixels.

For a given master camera, the 2D spline representations of the vortex segments were discretized with step sizes of between 5 and 10 pixels. Each of the resulting points was projected as an epipolar line in the image planes of all other cameras, as shown for camera 2 in Fig. 7, with two example epipolar lines from camera 5. The intersection points of the epipolar lines with the corresponding 2D vortex projections (blue curves in Fig. 7) were computed and used in the reconstruction process. During the point pairing, some difficulties arose; despite the preselection and coding of vortices, false pairing between non-corresponding vortex segments could not always be prevented, as illustrated for the upper red epipolar line in Fig. 7. Furthermore, the intersection between epipolar lines and wave-shaped vortex curves produced up to four distinct intersection points on a single vortex segment, as depicted for the lower epipolar line in Fig. 7. Some of the false intersection points were directly removed by comparing their position with polynomial fits based on adjacent points. The remaining false point pairs were filtered out in the spatial domain after reconstruction.

Due to the layout of the test site, the cameras were predominantly horizontally separated, which led to epipolar
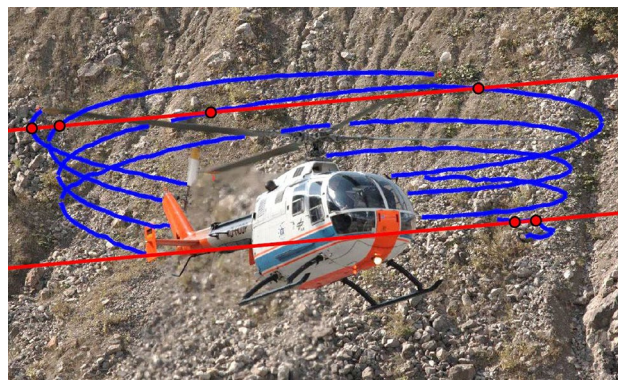

Fig. 7 Picture of the BO 105 from camera 2 with overlaid *blue vortex curves*, *red epipolar lines* as projected from camera 5, and multiple intersection points

lines with moderate inclination angles of around 10° (see Fig. 7). Some segments of the blade–tip vortices also had a mainly horizontal orientation and intersected with the epipolar lines at shallow angles, which reduced the horizontal accuracy of the respective point pairing.

4.3 Vortex reconstruction

A coordinate system for the vortex reconstruction was introduced at the instantaneous rotor hub position, as shown in Fig. 8. The y axis of the coordinate system was defined parallel to the horizontal component of the orientation vector of camera 1, directed away from camera 1. The z axis was oriented along the positive vertical direction. The x axis was defined orthogonal to the other axes to complete the Cartesian coordinate system.

A triangulation-based stereo photogrammetry technique was applied for the 3D reconstruction of the object-space vortices. As this method is point based, the discretized 2D point pairs produced by the epipolar geometry method were reconstructed instead of the continuous vortex curve. Some vortices were not captured by a single master camera and therefore were not reconstructable, hence two different master cameras 1 and 5 were used in order to increase the number of reconstructed vortex points.

The master cameras were paired with the other cameras and for each camera pair, a 3D point cloud was generated, representing the object-space vortices. The agglomeration of these point clouds exhibited scattering due to false point pairing, multiple intersection locations, and the remaining inaccuracy of the camera calibration. Points with a distance greater than 0.2 m from the median point center at the corresponding azimuthal position were treated as outliers and deleted. A second routine proceeded along sets of contiguous 3D vortex points and filtered out points with a deviation of more than

Fig. 8 Different perspectives **a–c** of the BO 105 in ascending hovering flight and reconstructed main rotor vortex system, as depicted in Fig. 5. Radial section **d** at the position marked in **c**. The colors of the vortices are the same as in Fig. 5
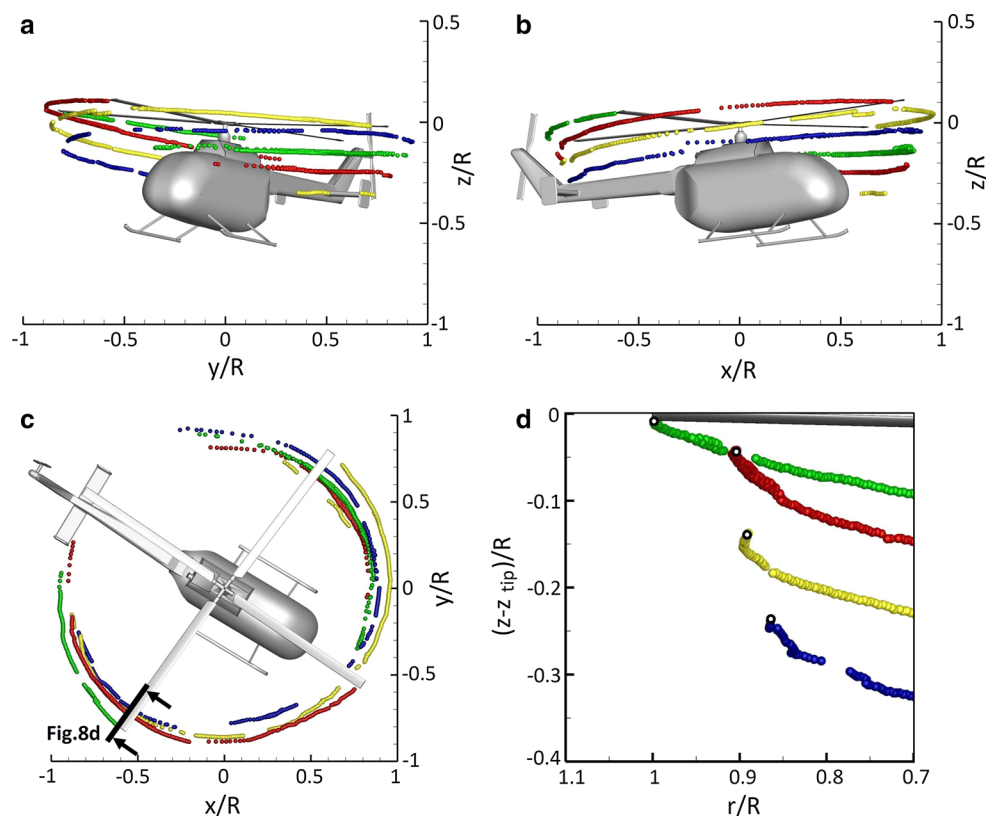
0.1 m from the predicted vortex line. Smaller fluctuations were caused by the variation of the master camera, which affected the point-pairing process and altered the intersection angles between the epipolar lines and the vortex curves. Thus, the horizontal accuracy was increased in some parts of the wake and decreased in others. A maximum of six individual 3D vortex systems could be reconstructed for a single master camera and six paired cameras, with a residual point scattering of about ±0.02 m around the average position. For two master cameras, the number of solutions doubled and the point scattering increased at some locations, leading to fluctuations of up to ±0.05 m.

The complete vortex reconstruction process employed in the present paper requires a processing time on the order of 50 h for a set of 7 measurement images. The majority of the applied routines do not significantly contribute to this duration and require negligible manual input. The processing time is mainly affected by the iterative camera calibration and filtering of erroneous vortex positions in the spatial domain. An acceleration of the processing can be achieved by replacing the elaborate iterative camera calibration with a standard camera calibration employing a calibration target. This measure, in combination with larger vertical distances between the cameras, positively affects the number of outliers in the reconstructed spatial domain and therefore the corresponding post-processing time.

4.4 Multi-camera 3D vortex reconstruction

Based on the iteratively optimized camera calibration, a 3D reconstruction was carried out for the 2D data set shown in Fig. 5. Multiple views of the reconstructed 3D vortex system are depicted in Fig. 8. The axes of the previously defined coordinate system are normalized with the rotor radius R. As for Fig. 5, the vortices are color-coded according to the blade they trail from. Figure 8 also features a 3D computer model of the BO 105, which is positioned according to the reconstructed points on the real helicopter fuselage. The rotor blades are also positioned based on the reconstructed locations of the blade–tips. Compared with the other reconstructed object-space points, the accuracy of the azimuthal blade–tip positions is reduced due to motion blurring and the residual camera jitter in combination with the high blade–tip velocity. These influences lead to a noticeably increased uncertainty in the azimuthal position of the blade–tips of around ±0.2c.

In Fig. 8a, b, the BO 105 is shown from perspectives close to camera 5 and camera 1, respectively. Fig. 8c shows the top view of the vortex system. As previously described, the vortex system acquired corresponds to an ascending hover flight state. The BO 105 performed a swinging motion along the vertical axis to generate higher maneuvering loads. The images were taken close to the bottom reverse point of the maneuver, where the vertical

Fig. 9 Comparison of corresponding views of **a** the experimental data set shown in Fig. 8 and **b** result from an unsteady 3D free-wake panel code simulation of a similar flight state
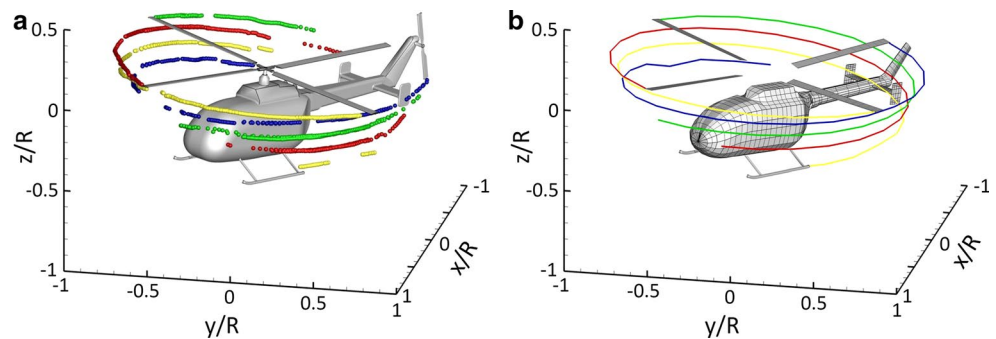
acceleration and the blade loading were highest. Due to the unsteady maneuver, the fuselage of the helicopter had an inclination of about 6° and a roll angle of −2°, as visible in Fig. 8.

The reconstructed 3D vortex curves closely resemble the 2D projections shown in Fig. 5. The characteristic contraction of the rotor wake that was already described in Fig. 5 is also evident in the 3D plots, especially in the top view, shown in Fig. 8c. The initial large radial convection of the young vortices close to the rotor is observable, e.g., for the red vortex curve shed by the forward facing blade. The strongest radial convection is found for the initial 20° behind the forward facing blade and differs from the moderate and steady radial convection of the young vortices in other azimuthal regions of the wake. This inhomogeneity can be attributed to the unsteady flight condition and the control inputs of the pilot in order to keep the helicopter within the measurement volume. For older vortex ages, the azimuthal asymmetry decreases and the characteristic helical shape of the vortex system develops. Some parts of the wake are covered by multiple cameras, enabling the reconstruction of continuous vortex filaments with an azimuthal span of about 90° (see e.g., the yellow vortex line behind the retreating blade in Fig. 8). Other vortices exhibit gaps due to the filtering of outliers, as described in the previous sections. For regions that are only covered by a single camera, the reconstruction of 3D vortices is not possible, as can be observed for the region on the left-hand side of the tail boom in the 2D images of Fig. 5, where the green vortex segment is only imaged by camera 1. The monoscopic coverage of parts of the wake can be attributed to the moderate horizontal angle of 80° between the outermost cameras and the obstructed view caused by the fuselage and the exhaust gases.

The green vortex curve visible in the front of Fig. 8a exhibits increased scattering of up to ±0.05 m for vortex ages of between 210° and 260°. The scattering at this location corresponds to the small intersection angles below 5° in the epipolar point-pairing process. The small angles are due to the mainly horizontal orientation of the corresponding vortices in the lower camera images and missing line segments in the upper camera images. Thus, the effectiveness of the vertical camera separation is decreased for this vortex filament and becomes insufficient for an accurate 2D point pairing.

For the present flight state illustrated in Figs. 5 and 8, macroscopic instability effects can only be observed for vortex ages close to $\psi_v = 360°$, as depicted in Fig. 5 on the lower right side of camera images 2–5. The corresponding vortex could not be completely reconstructed due to its missing projections in the images of cameras 1 and 6 as well as the limited overlap between the line segments visualized by the other cameras. Therefore, the wavy shape of the vortex was only partially captured.

A radial cut through the vortex system of Fig. 8c at the marked trailing edge position of the advancing blade is depicted in Fig. 8d. The radial position r is normalized with the rotor radius R. The vertical coordinate z is plotted relative to the height z_{tip} of the advancing blade–tip and normalized with R. The intersection locations of four vortex curves with the sectional plane are marked by black circles and visualize the outline of the contracting wake. The green vortex curve is shed by the blade visible at the top of Fig. 8d and intersects with the sectional plane right behind the tip of the trailing edge. Although helicopter rotors operated in hovering flight are generally not prone to BVI effects, important geometric parameters for BVI can be determined in the present case. The minimum miss distance between the red vortex and the advancing blade is quantified as $0.8c$ at a location of $r/R = 0.905$ with an interaction angle of close to 90°.

The aim of the present study was to demonstrate the capability of the BOS technique to localize large-scale 3D vortex systems. As a test of proof-of-concept, therefore, an elaborate recording of the pilot control inputs and rotor boundary conditions, which are required for a quantitative comparison with numerical of experimental results, was deemed not necessary to fulfill the purpose of the current flight tests. With the information available for the present experiment, an outlook for a future application of the experimentally determined 3D vortex positions was able to be prepared and is given in Fig. 9. Figure 9 shows a

qualitative comparison between corresponding views of the reconstructed experimental data set (Fig. 9a) and the result of a numerical simulation of the flow field and vortex system around the BO 105 (Fig. 9b). The numerical simulation was carried out using the incompressible, unsteady 3D free-wake panel method solver UPM (Yin and Ahmed 2000; Yin 2012). UPM is a velocity-based, indirect potential formulation that uses a combination of source and dipole distributions on the rotor blades. In the rotor wake, dipole panels and a full-span free-wake model including a tip-vortex roll-up formulation are applied for the computation of the vortex system. Rigid blades were assumed for the simulation and adjusted with a force trimming procedure to achieve a rotor thrust of $T = 25\,\text{kN}$ and a vertical climb velocity of $1\,\text{m/s}$. Figure 9b depicts a fuselage model of the BO 105 and the computed blade tip vortices. Vortex visibility was matched with the experimental result in Fig. 9a. Good qualitative agreement is found between the experimental and numerical results with a very similar shape of the vortex system. In detail, some differences in the wake contraction and vortex disturbance levels are observed, which are mainly attributed to the unavailable or estimated experimental boundary conditions and the temporal resolution of the numerical simulation. Despite these differences, the overall agreement between the results shown in Fig. 9 underlines the quality and comparability of the experimental data and gives an outlook for potential applications of future 3D BOS results with well-determined boundary conditions.

5 Conclusions

The blade–tip vortices of a BO 105 helicopter were visualized using a 10-camera BOS measurement system with a natural background. The test environment in an open-pit mine allowed for the execution of unsteady maneuvers around the hovering flight condition. During a swinging motion around the pitch axis, blade–tip vortices were visualized up to a vortex age of $\psi_v = 450°$, and smooth sinuous disturbance effects were observed. For an ascending flight maneuver, a maximum vortex age of $\psi_v = 360°$ and only isolated vortex instability effects were observed.

The detected vortices were semiautomatically extracted from the measurement images and discretized. Due to the large dimensions of the test site with camera-background distances of up to 300 m and a measurement volume located up to 18 m above the ground, a favorable camera calibration with a calibration target was not realized. Instead, the camera setup was initially calibrated based on measurements of the geometric layout. The calibration was iteratively optimized based on 44 prominent points on the helicopter fuselage. Correspondence between 2D points on the recorded vortex filaments in multiple camera images was established using epipolar geometry. Due to the layout of the test site, the cameras were mainly horizontally separated with an angle of 80° between the outermost cameras, compared with 6° in the vertical direction. The corresponding intersection angles between the epipolar lines and the vortices were shallow and in some cases smaller than 10°, leading to deviations and defects in the point-pairing process.

The object-space points on the helicopter and the vortices were reconstructed using a triangulation-based stereo photogrammetry technique. Seven of the ten available cameras were used for the reconstruction; the other three cameras were not used due to unsuitable backgrounds and lighting conditions. The reconstructed calibration points on the helicopter fuselage and the majority of the reconstructed vortex points scattered by less than ±0.03 m around the mean position. For some parts of the 3D vortex system, the deviations in the point-pairing process resulted in an increased point scattering of up to ±0.05 m as well as obvious outliers that were filtered out. Some additional gaps around the tail boom resulted from the view obstructed by the helicopter fuselage and the exhaust from the engines in combination with the restricted camera perspectives.

The present setup allowed for the reconstruction and analysis of the main part of the helicopter's vortex system during ascending hovering flight. Direct comparison with the result of an unsteady 3D free-wake panel code simulation showed good qualitative agreement with small differences due to unavailable experimental parameters. From a radial section of the experimental data set, important geometric parameters for BVI were determined, such as the minimum blade–vortex miss-distance of 0.8 chord lengths at a position of $r/R = 0.905$ with an interaction angle of 90°. These results demonstrate the potential of the multi-camera BOS method in the investigation of rotorcraft aerodynamics and BVI effects.

References

Bauknecht A, Merz CB, Raffel M (2014a) Airborne application of the background oriented Schlieren technique to a helicopter in forward flight. In: 17th int. symp. on applications of laser techniques to fluid mechanics, Lisbon, Portugal, 07–10 July, 2014

Bauknecht A, Merz CB, Raffel M, Landolt A, Meier AH (2014b) Blade–tip vortex detection in maneuvering flight using the background-oriented schlieren technique. J Aircraft. doi:DOIurl10.2514/1.C032672

Fischler MA, Bolles RC (1981) Random sample consensus: a paradigm for model fitting with applications to image analysis and automated cartography. Commun ACM 24(6):381–395

Hardin JC, Lamkin SL (1987) Concepts for reduction of blade/vortex interaction noise. J Aircraft 24(2):120–125

Hartley R, Zisserman A (2003) Multiple view geometry in computer vision. Cambridge university press, Cambridge

Hartley RI (1997) In defense of the eight-point algorithm. IEEE Trans Pattern Anal Mach Intell 19(6):580–593

Heineck JT, Kushner LK, Schairer ET (2013) Measurements of tip vortices from a full-scale UH-60A rotor by retro-reflective background oriented schlieren and stereo photogrammetry. In: American Helicopter Society 69th Annual Forum, Phoenix, AZ, USA

Kindler K, Goldhahn E, Leopold F, Raffel M (2007) Recent developments in background oriented Schlieren methods for rotor blade tip vortex measurements. Exp Fluids 43:233–240. doi:10.1007/s00348-007-0328-9

Kindler K, Mulleners K, Richard H, van der Wall BG, Raffel M (2011) Aperiodicity in the near field of full-scale rotor blade tip vortices. Exp Fluids 50(6):1601–1610. doi:10.1007/s00348-010-1016-8

Klinge F, Hecklau M, Raffel M, Kompenhans J, Göhmann U (2006) Measurement of the position of rotor blade vortices generated by a helicopter in free flight by means of stereoscopic background oriented schlieren method (BOS). In: 13th intl. symp. on applications of laser techniques to fluid mechanics, Lisbon, Portugal

Kutz BM, Keßler M, Krämer E (2013) Experimental and numerical examination of a helicopter hovering in ground effect. CEAS Aeronaut J 4(4):397–408. doi:10.1007/s13272-013-0084-x

Lim JW, Strawn RC (2008) Computational modeling of HART II blade–vortex interaction loading and wake system. J Aircraft 45(3):923–933

Meyn LA, Bennett MS (1993) Application of a two camera video imaging system to three-dimensional vortex tracking in the 80-by 120-foot wind tunnel. In: AIAA 11th applied aerodynamics conference, Monterey, CA, USA

Mikhail EM, Bethel JS, McGlone JC (2001) Introduction to modern photogrammetry, vol 1. Wiley, New York

Raffel M, Tung C, Richard H, Yu Y, Meier GEA (2000) Background oriented stereoscopic schlieren for full-scale helicopter vortex characterization. In: 9th int. symp. on flow visualization, Edinburgh, Scotland

Raffel M, Willert CE, Wereley ST, Kompenhans J (2007) Particle image velocimetry: a practical guide. Springer, Berlin

Raffel M, Heineck JT, Schairer E, Leopold F, Kindler K (2014) Background-oriented schlieren imaging for full-scale and in-flight testing. J Am Helicopter Soc 59(1):1–9. doi:10.4050/JAHS.59.012002

Richard H, Raffel M (2001) Principle and applications of the background oriented schlieren (BOS) method. Meas Sci Technol 12(9):1576–1585. doi:10.1088/0957-0233/12/9/325

Splettstoesser WR, Kube R, Wagner W, Seelhorst U, Boutier A, Micheli F, Mercker E, Pengel K (1997) Key results from a higher harmonic control aeroacoustic rotor test (HART). J Am Helicopter Soc 42(1):58–78

Sullivan JP (1973) An experimental investigation of vortex rings and helicopter rotor wakes using a laser doppler velocimeter. Tech. rep., MIT Technical Report 183, June, 1973

van der Wall BG (2012) Extensions of prescribed wake modelling for helicopter rotor BVI noise investigations. CEAS Aeronaut J 3(1):93–115. doi:10.1007/s13272-012-0045-9

van der Wall BG, Burley CL, Yu YH, Pengel K, Beaumier P (2004) The HART II test—measurement of helicopter rotor wakes. Aerosp Sci Technol 8(4):273–284. doi:10.1016/j.ast.2004.01.001

Venkatakrishnan L, Meier GEA (2004) Density measurements using the background oriented schlieren technique. Exp Fluids 37:237–247. doi:10.1007/s00348-004-0807-1

Wadcock AJ, Yamauchi GK, Solis E, Pete AE (2011) PIV measurements in the wake of a full-scale rotor in forward flight. In: 29th AIAA applied aerodynamics conference. Honolulu, HI, USA, pp 1874–1896

Yin J (2012) Main rotor and tail rotor blade vortex interaction noise under the influence of the fuselage. In: 38th European rotorcraft forum, Amsterdam, The Netherlands

Yin J, Ahmed SR (2000) Helicopter main-rotor/tail-rotor Interaction. J Am Helicopter Soc 45:293–302